



Synthesis of a core-shell heterostructured MoS₂/Cd_{0.9}Zn_{0.1}S photocatalyst for the degradation of diclofenac under visible light



Meixuan Cai^a, Ruobai Li^a, Zhijie Xie^a, Jiaxing Huang^a, Yongqin Zeng^a, Qianxin Zhang^a, Haijin Liu^b, Wenying Lv^{a,*}, Guoguang Liu^a

^a School of Environmental Science and Engineering, Guangdong University of Technology, Guangzhou, 510006, China

^b School of Environment, Henan Normal University, Henan Key laboratory for Environmental Pollution Control, Xinxiang, 453007, China

ARTICLE INFO

Keywords:

Photocatalytic degradation
MoS₂ modified Cd_xZn_{1-x}S
Diclofenac
Reactive species
Transformation pathways

ABSTRACT

The development of novel noble metal-free semiconductor catalysts with high photocatalytic efficiency is of great importance toward the degradation of organic compounds. In this work, a core-shell heterojunction MoS₂/Cd_{0.9}Zn_{0.1}S photocatalytic material was successfully synthesized via a simple one-step hydrothermal method. The introduction of MoS₂ led to a significant improvement in the photocatalytic degradation of diclofenac (DCF). It was confirmed that 0.1% loading content of MoS₂ achieved an optimal photocatalytic efficiency of 86% in the degradation of DCF under visible light irradiation, which was 1.8 times higher than that of Cd_{0.9}Zn_{0.1}S. The MoS₂/Cd_{0.9}Zn_{0.1}S heterostructured composites possessed improved photocatalytic properties, which implied that the combination of Cd_{0.9}Zn_{0.1}S and MoS₂ shortened the carrier transport pathway and facilitated the separation efficiency of electrons and holes. Reactive species (RS) scavenging experiments and electron spin resonance (ESR) demonstrated that superoxide radicals (O₂^{·-}) and electron holes (h⁺) played predominant roles throughout the DCF degradation process. The primary intermediates were explored through HRAM LC/MS/MS, and a transformation pathway was tentatively proposed. This study promoted the application of an economical, highly efficient and visible light driven MoS₂ co-catalyst for the degradation of organic contaminants.

1. Introduction

As emerging organic micropollutants, Pharmaceutical and Personal Care Products (PPCPs), have garnered broad attention, particularly pharmaceutical compounds that include various antibiotics, painkillers, blood pressure medications, hypnotics, etc. [1]. Diclofenac (DCF) is one of the most commonly used anti-inflammatory drugs, which has increasingly been detected in sewage treatment plant (STP) effluent, groundwater, and ambient waterways. The detected concentrations of DCF in STP effluent, groundwater, and surface water are 4.7 ug/L [2], 0.59 ug/L [3], and 1.2 ug/L [4], respectively. Despite its relatively low concentration, the presence of DCF in water poses a large menace to human and aquatic health due to its longevity and biological toxicity. However, only 30% of DCF was removed by conventional sewage water treatment plant due to its low biodegradability and adsorption characteristics in activated sludge [5]. Many approaches have been investigated and developed for the removal of contaminants, such as ozonation [6], Fenton oxidation [7], UV/H₂O₂ [8], and photocatalytic degradation [9,10]. Among them, photocatalytic materials can exploit solar energy and are feasible to integrate into systems without the

addition of chemical reagents or application of external electric energy [11,12]. Some researchers have used photocatalytic materials to make photoelectrocatalytic microreactor [13,14], combine with advanced oxidation processes (AOPs) [15] or construct heterostructured photocatalyst [16] for the organic pollutant degradation and achieve certain achievements. Therefore, they are expected to enable efficacious strategies for the removal of DCF from water.

Recently, scientific and engineering interest in the application of semiconducting photocatalysts has grown exponentially, due to their high utilization of visible sunlight and degradation efficiencies [17]. As a well-known semiconductor, cadmium sulfide (CdS), is one of the most promising sulfide because of its low cost, thermochemical stability, and noble metal-free properties. Its band gap of 2.4 eV makes it possible to capture solar energy for the degradation of organic contaminants [18,19]. Unfortunately, the application of CdS in photocatalytic degradation was hampered by the rapid recombination of photogenerated charge carriers and photocorrosion. [20,21]. In previous studies, MNP loading on CdS surfaces [22,23], combination with metallic oxide (Fe₂O₄ [24], CuO [25]), and hybridization with other metal sulfides (Cd_xZn_{1-x}S [26], Cd_xMn_{1-x}S [27], Cd_xLa_{2(1-x)}S₄ [28], Cd_{0.1}Sn_xZn_{0.9-2x}S

* Corresponding author.

E-mail address: lvwy612@163.com (W. Lv).

[29]) were investigated to boost photocatalytic efficiencies. Of these, synergies with other metal sulfides were shown to be a practical method for enhancing photocatalytic efficiency and photostability. A $\text{Cd}_x\text{Zn}_{1-x}\text{S}$ solid solution exhibited superior photocatalytic activity over CdS , due to its valence band being regulated by altering the size of x to meet the requirements of absorbing visible light for the destruction of organic contaminants [30]. For instance, Li et al. found that a $\text{Cd}_x\text{Zn}_{1-x}\text{S}$ sample demonstrated greater photocatalytic activity for the degradation of dyes by adjusting the Zn/Cd ratio [31]. Although photocatalytic activity can be enhanced by changing x to regulate the valence band, the photocatalytic efficiency of $\text{Cd}_x\text{Zn}_{1-x}\text{S}$ still suffered from the rapid recombination of electron-hole pairs. Consequently, it is imperative to further explore the $\text{Cd}_x\text{Zn}_{1-x}\text{S}$ system based on co-catalyst modification under visible light irradiation for augmenting the photocatalytic degradation rate.

Considerable effort has been devoted to improving the separation efficiencies of photogenerated electron-hole pairs through Ni_2P loading [32] and the modification of other semiconductors such as C_3N_4 [33] and MoS_2 [34,35]. Recently, the transition metal sulfide MoS_2 (a low-cost, noble metal-free, nontoxic co-catalyst), has been used for a wide range of applications in photocatalysis [21,36]. MoS_2 is comprised of two S atom layers interspersed with a Mo atom layer, where the basal plane of saturated S atoms stabilizes the bulk MoS_2 [37]. Not only does MoS_2 provide abundant active sites stemming from its sulfur edge, but also serves as an electron receiver to restrain the recombination of electron-hole pairs in the photocatalytic degradation of pollutants [38–40]. Considering the matching band gaps of various layered semiconductors with $\text{Cd}_x\text{Zn}_{1-x}\text{S}$, MoS_2 should be suitable for the synthesis of 2D core-shell heterostructures with $\text{Cd}_x\text{Zn}_{1-x}\text{S}$ [34]. However, as far as we known, there no work has yet been performed on the synthesis of $\text{Cd}_{0.9}\text{Zn}_{0.1}\text{S}$ as a light harvester and MoS_2 as a co-catalyst for the degradation organic pollutant. Accordingly, we proposed to create a series of $\text{Cd}_x\text{Zn}_{1-x}\text{S} @ \text{MoS}_2$ photocatalytic composites to increase the efficacy of DCF removal from water.

For the present study, a $\text{Cd}_x\text{Zn}_{1-x}\text{S}$ solid solution was initially synthesized via a simple one-step hydrothermal approach, which showed the highest photocatalytic degradation rate of $x = 0.9$. Hence, the $\text{Cd}_{0.9}\text{Zn}_{0.1}\text{S}$ sample was employed in the following experiment. The $\text{Cd}_{0.9}\text{Zn}_{0.1}\text{S}/\text{MoS}_2$ photocatalyst exhibited significantly improved visible-light photocatalytic activity for the degradation of DCF, in contrast to pure $\text{Cd}_{0.9}\text{Zn}_{0.1}\text{S}$. The morphologies, light absorption levels, and spectral characteristics of $\text{Cd}_{0.9}\text{Zn}_{0.1}\text{S}/\text{MoS}_2$ composites were systematically investigated. Furthermore, the reactive species involved in this photocatalytic system were determined via electron spin resonance and subsequently a plausible reaction mechanism was proposed.

2. Experimental

2.1. Materials

Cadmium acetate dehydrate ($\text{Cd}(\text{CH}_3\text{COOH})_2 \cdot 2\text{H}_2\text{O}$), zinc acetate ($\text{Zn}(\text{CH}_3\text{COOH})_2 \cdot 2\text{H}_2\text{O}$), sodium molybdate dehydrate ($\text{Na}_2\text{MoO}_4 \cdot 2\text{H}_2\text{O}$), and thioacetamide (TAA) were purchased from Aladdin Co. Ltd. (Shanghai China). The DCF was obtained from J & K Chemical Co. Ltd. (Beijing, China). The reagents used in the experiments were analytical grade and required no further purification.

2.2. Preparation of $\text{Cd}_x\text{Zn}_{1-x}\text{S}$ and $\text{MoS}_2/\text{Cd}_x\text{Zn}_{1-x}\text{S}$ composites

Pure $\text{Cd}_{0.9}\text{Zn}_{0.1}\text{S}$ was synthesized via a one-step hydrothermal route [41]. $\text{Cd}(\text{CH}_3\text{COOH})_2 \cdot 2\text{H}_2\text{O}$ (8.1 mmol), $\text{Zn}(\text{CH}_3\text{COOH})_2 \cdot 2\text{H}_2\text{O}$ (0.9 mmol), and TAA (35 mmol) were dispersed into 40 mL of ultrapure water, followed by 30 min of stirring. Subsequently, the mixed liquor was transferred to a 100 mL capacity Teflon-lined stainless steel autoclave for 24 h at 160 °C. Finally, the $\text{Cd}_{0.9}\text{Zn}_{0.1}\text{S}$ solid solution was collected by centrifuging at 10,000 rpm for 8 min after cooling to room

temperature. The precipitate was rinsed three times with distilled water and dried at 80 °C for 16 h. The $\text{Cd}_x\text{Zn}_{1-x}\text{S}$ material was synthesized following the same process described above with a controlled ratio of Cd to Zn atoms. The $\text{MoS}_2/\text{Cd}_x\text{Zn}_{1-x}\text{S}$ composites were prepared via a facile thermo polymerization method. $\text{Cd}(\text{CH}_3\text{COOH})_2 \cdot 2\text{H}_2\text{O}$ (8.1 mmol), $\text{Zn}(\text{CH}_3\text{COOH})_2 \cdot 2\text{H}_2\text{O}$ (0.9 mmol), and TAA (35 mmol) were dissolved into 40 mL DI water. After stirring for 30 min, different molar ratios of Na_2MoO_4 (0 wt%, 0.05 wt%, 0.1 wt%, 0.2 wt%, 0.5 wt %) were added to the solution above under continuous stirring for 60 min. Subsequently, the suspension was transferred to a 100 mL capacity Teflon-lined stainless autoclave and stored at 210 °C for 24 h. Following centrifugation at 10,000 rpm for 20 min, the obtained precipitate was rinsed three times with DI water and dried in an oven at 80 °C for 16 h.

2.3. Characterization

XRD patterns were obtained by X-ray diffraction (XRD, BrukerAXS, D8Advance), which were employed to characterize the crystal structure of the samples with $\text{Cu K}\alpha$ radiation, at a scanning rate of 5°/min., from 10° to 80°. Scanning electron microscopy (SEM) images were received using a Hitachi SU8220. Transmission electron microscopy (TEM, Thermo, Talos F200S) was employed to elucidate the crystal planes and fringes of the samples. The elemental composition was acquired through X-ray photoelectron spectroscopy (XPS, Escalab 250Xi) with an achromatic Mg-K α radiation as the excitation source. The Brunauer-Emmett-Teller (BET) surface area and porosity measurements were conducted via N_2 adsorption-desorption isotherms. The spectra of the materials were scanned using a UV-vis spectrophotometer (UV-3600 Plus, SHIMADZU). The photoluminescence (PL) spectra of the solid samples were obtained by a FluoroMax-4 fluorescence spectrophotometer (HORIBA Jobin Yvon) with an excitation of 350 nm. The transient photocurrent responses, electrochemical impedance spectra (EIS), and Mott-Schottky plots were measured via an Electrochemical Workstation (Multi Autolab/204, Metrohm Autolab B.V.). The zero potential was tested with a zeta potential analyzer (Zetasizer NANO ZS, Malvern). The atomic ratio of $\text{Cd}^{2+} : \text{Zn}^{2+}$ in the $\text{Cd}_x\text{Zn}_{1-x}\text{S}$ materials and the actual loading content of MoS_2 on $\text{Cd}_{0.9}\text{Zn}_{0.1}\text{S}$ were tested via ICP-OES (PerkinElmer NexION 300X). Electron spin resonance (ESR) was utilized to quantitatively analyze the active substances in the reactions.

2.4. Photocatalytic activity texts

2.4.1. Photocatalytic performance

Photocatalytic experiments were conducted using a XPA-7 rotary photochemical reactor (Nanjing). We employed a 350 W Xe-lamp with a 420 nm cut-off filter as a visible light irradiation source for each test. The optical density of visible light radiated on the photocatalyst was measured to be 1.553 mW/cm^2 by the Full-spectrum bright light power meter (CEL-NP2000). The illuminated area was 39.6 cm^2 (18 cm * 2.2 cm) and the distance between the liquid level and light source was 5 cm. Initially, the photocatalysts (25 mg) were dispersed in a 50 mL aqueous DCF solution (20 μM). Subsequently, the suspension was magnetically stirred for 30 min in the dark to attain adsorption-desorption equilibrium. Under continued magnetic stirring and exposure to light 1.0 mL of the solution was extracted at fixed time intervals and filtered through 0.45 μm Millipore filters to remove the catalyst. The concentration of DCF was characterized by high performance liquid chromatography (HPLC). The DCF degradation intermediate products were analyzed by ultrahigh-performance liquid chromatography (UPLC) with triple quadrupole mass spectrometry (Thermo Fisher, America). Meanwhile, the total organic carbon (TOC) was recorded using a TOC-VCPh analyzer to compare its mineralization in solution (Shimadzu, Japan).

2.4.2. Electrochemical measurements

Electrochemical measurements were performed via a CHI-660 electrochemical system equipped with a standard 3-electrode system. The platinum (Pt) wire and saturated calomel electrode (SCE) were used as the counter and the reference electrodes, respectively. The photoanode was prepared as follows: Indium tin oxide (ITO) glass was cleaned by continuous washing with ultra-pure water and ethanol for 30 min in ultrasonic instrument. Subsequently, 1 mg photocatalyst was dispersed in a mixed solution containing 10 µl Nafion and 1 ml ethanol for ultrasonic treatment for 30 min. The prepared suspension was dripped onto the ITO glass surface to form an uniformly exposed area, dried overnight in an oven at 60 °C. Finally, the prepared ITO glass was placed in 0.1 M sodium sulfate solution (Na_2SO_4) and illuminated with 450 nm LED lamp to record the photocurrent.

2.4.3. Determination of RSs

Quenching experiments were used to identify the free radicals that were generated during the DCF degradation process. Several quenching agents (e.g., isopropanol (IPA, 100 mM), benzoquinone (BQ, 1 mM), sodium oxalate ($\text{Na}_2\text{C}_2\text{O}_4$, 10 mM)) were employed as hydroxyl radical ($\cdot\text{OH}$), superoxide ($\text{O}_2^{\cdot-}$), and hole (h^+) scavengers [42,43]. The electron spin resonance (ESR) technique with DMPO spin-trapped radicals were employed for the quantitative analysis of hydroxyl radical ($\cdot\text{OH}$) and superoxide ($\text{O}_2^{\cdot-}$) reactive species, passing through a JESFA200 electron paramagnetic resonance spectrometer.

2.4.4. Detection and identification of DCF and transformation products

Residual concentrations of DCF were detected using high performance liquid chromatography (HPLC), which was equipped with a Hypersil C18 column (250 × 4.6 mm, 5 µm). The ratio of the mobile phase was comprised of 70% methyl alcohol and 30% formic acid (0.2%) at a detection wavelength of 276 nm. The intermediate products in the DCF degradation process were identified by a HPLC system (Ultimate 3000RSLC, Thermo Scientific, USA) and a Q Exactive Orbitrap mass spectrometer. A Hypersil GOLD C18 (100 × 2.1 mm, 1.9 µm) was employed to separate the byproducts. Detailed information on the HRAM LC/MS/MS is listed in Tables S1and S2.

3. Results and discussion

3.1. Morphology and phase structure characteristics

The structural features of the 0.1% MoS₂ (0.1 M) Cd_{0.9}Zn_{0.1}S (CZS) compound were acquired through SEM. According to Fig. 1a, the 0.1 M CZS composite revealed a 2D lamellar structure that tended to be smooth and regular. The core-shell heterostructures between the MoS₂ and Cd_{0.9}Zn_{0.1}S were verified by using HRTEM (Fig. 1b–d). The unambiguous lattice fringes of the 0.1 M CZS with a spacing of 0.315 nm (Fig. 1d) could be attributed to the crystal plane of Cd_{0.9}Zn_{0.1}S [44]; the elemental mapping images in Fig. 1d show that Cd, Zn, and S were evenly distributed. Furthermore, the weak Mo signal was accorded to the structure of the 0.1 M CZS surface layer [45], which further confirmed the formation of MoS₂/Cd_{0.9}Zn_{0.1}S core-shell heterojunctions. From the TEM image, the intimate contact between Cd_{0.9}Zn_{0.1}S and MoS₂ component was observed, which was beneficial for the electron transfer between two phases. In addition, the MoS₂ was grown on the Cd_{0.9}Zn_{0.1}S outside surface, which provided abundant reaction sites for photocatalytic reactions, thus enhancing the photocatalytic performance [46].

The XRD patterns of the as-prepared Cd_{0.9}Zn_{0.1}S and MoS₂/Cd_{0.9}Zn_{0.1}S heterostructures with different MoS₂ contents were recorded on Fig. 2. In contrast to the standard CdS (JCPDS No.65-3414) [47] and ZnS (JCPDS No.77-2100) [48] diffraction peaks, the characteristic Cd_{0.9}Zn_{0.1}S diffraction peaks were shifted in the XRD patterns. It was clear that the as-prepared specimens were not simple mixtures of CdS and ZnS but were owe to a Cd_{0.9}Zn_{0.1}S solid solution. The spectra

confirmed the crystalline structure of the photocatalyst Cd_{0.9}Zn_{0.1}S. The major diffraction peaks at 20 were consistent with the previous research (JCPDS card no. 00-040-0835) [49]. Upon MoS₂ loading, the MoS₂/Cd_{0.9}Zn_{0.1}S diffraction peak was not obvious shifted, and no additional MoS₂ peaks could be clearly identified. This may have been due to its low content and good distribution capacity, indicating little change of the CZS phase in the 0.1 M CZS composites [34]. The crystallite size of the MoS₂/Cd_{0.9}Zn_{0.1}S samples were calculated through the Debye-Scherrer formula $D = k\lambda/(\beta\cos\theta)$. In the formula, the various parameters, k, λ , β , θ , are expressed as the shape factor, X-ray wavelength, Peak FWHM and Diffraction angle, respectively. Due to the cubic crystal structure of the samples, the shape factor k was 0.943; the X-ray wavelength of the instrument was 0.154 nm and the peak FWHM should be converted to radians. From the result of calculation (Table S3), the intensities of the XRD peaks were weakened with lower MoS₂ ratios owing to a decreased gallery distance between the layers [50]. No other impurity phases were found in the XRD patterns of the composites, which suggested that the sample was a pure two-phase composite.

3.2. Physicochemical properties

The X-ray photoelectron spectrum was obtained to study the surface composition and chemical states of the 0.1 M CZS. The survey XPS spectrum (Fig. S1) of the 0.1% MoS₂/Cd_{0.9}Zn_{0.1}S verified the existence of Cd, Zn, S, and Mo. As shown in Fig. 3a, the Cd 3d of the 0.1 M CZS was split into two peaks at 404.1 eV and 410.8 eV, which were ascribed to Cd 3d_{5/2} and Cd 3d_{3/2} [41]. The Zn 2p spectrum (Fig. 3b) exhibited two strong auger electron peaks at 1021.1 eV, which belonged to Zn 2p_{3/2}, with a multiple split peak at 1023.6 eV and 1044.5 eV, associated with Zn 2p_{1/2} that had a multiple split peak of 1046.6 eV [30]. The high resolution S2p XPS spectrum (Fig. 3c) for the 0.1 M CZS appeared at 160.7 eV and 161.8 eV, which were well matched with the binding energies of S2p_{3/2} and S2p_{1/2} as described in previous reports [51]. The Mo 3d peaks observed at 227.7 eV and 231.4 eV corresponded to Mo 3d_{5/2} and Mo 3d_{3/2}, which meant that Mo⁴⁺ was the dominant valence state, which demonstrated the presence of MoS₂ [34]. Compared with the X-ray photoelectron spectrum of pure CZS, the binding energies of Cd 3d, Zn 2p, and S 2p uniformly shifted to lower binding energies of 0.8–1.0 eV. Briefly, these results implied that a strong interfacial contact between Cd_{0.9}Zn_{0.1}S and MoS₂ was established for the transfer of photogenerated electrons and holes [52,53]. The N₂ adsorption–desorption isotherms and the corresponding pore size distribution curves of the CZS and 0.1 M CZS are shown in Fig. 4, which exhibit type IV with H3 hysteresis loops in the P/P₀ range of from 0.9 to 1.0 [45]. The specific BET surface area of the CZS was 4.7253 m²/g, nevertheless the 0.1 M CZS surface area slightly increased from 4.7253 m²/g to 5.4367 m²/g. From these results, it could be concluded that MoS₂ was successfully loaded onto the CZS surface, which was beneficial in terms of increasing the population of active sites and photocatalytic activity. Further, the pore size distribution diagram depicted in Fig. 4, revealed the bulky aperture of two specimens (from 0 nm to 100 nm), indicating the existence of mesopores and macropores. The porous structure of the compounds provided a more accessible interface for the transfer of photogenerated electrons [54].

3.3. Analysis of optical properties

The optical properties of Cd_{0.9}Zn_{0.1}S/MoS₂ with different MoS₂ loadings were investigated through UV-vis diffuse reflectance spectra (UV-vis DRS). As depicted in Fig. 5a, pure Cd_{0.9}Zn_{0.1}S revealed an absorption edge at ~550 nm, which was recorded in previous reports [55]. Following hybridization with MoS₂, the composite exhibited a meaningful red-shift in contrast to Cd_{0.9}Zn_{0.1}S. In addition, due to the changes in the color of materials, from yellow to yellow-gray, the light absorption intensity of the compounds strengthened with increased MoS₂ in the range of visible and infrared absorption [34,56]. These

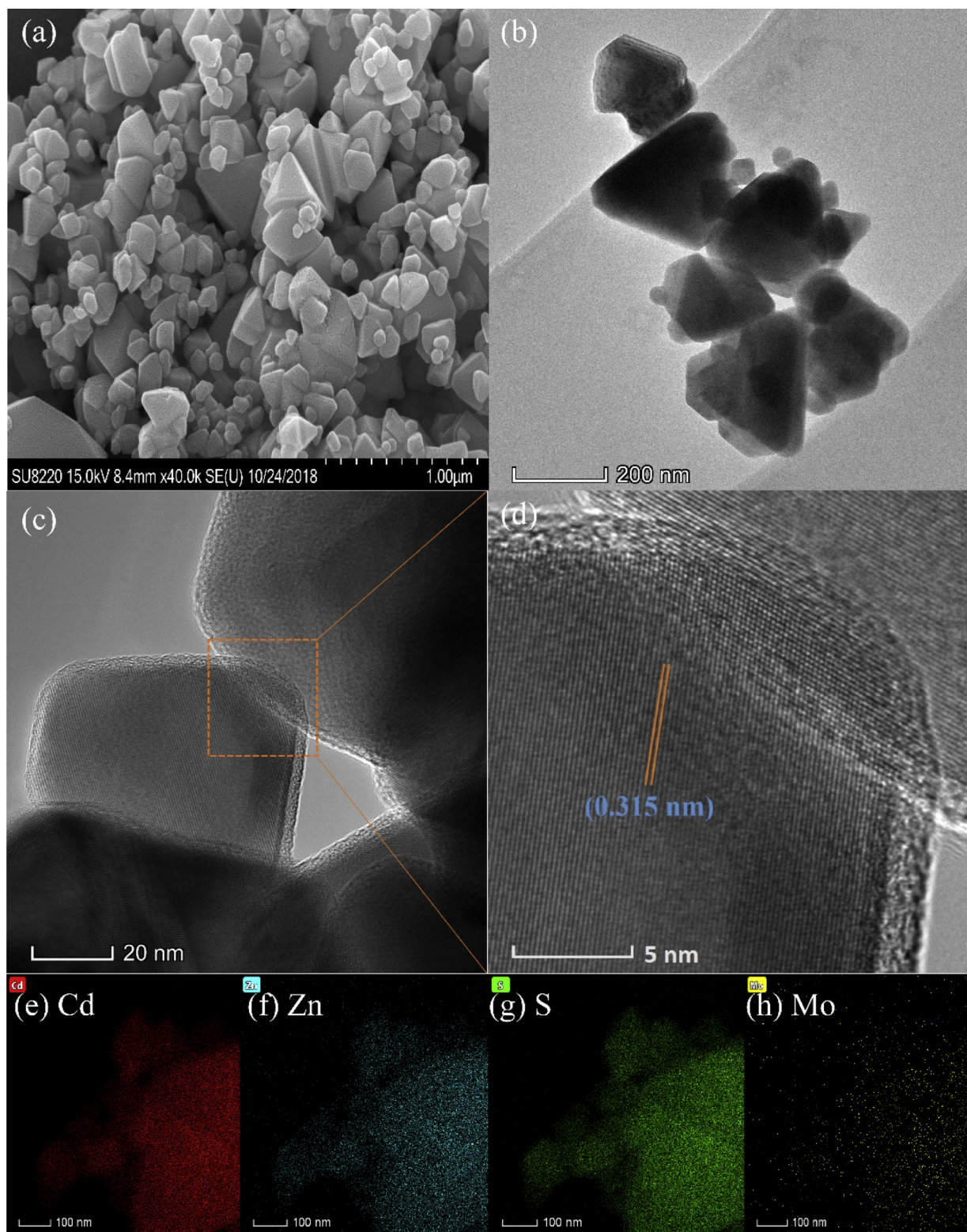


Fig. 1. (a) SEM, (b) TEM, (c) HRTEM and (d) the interplanar spacing images of 0.1%MoS₂/Cd_{0.9}Zn_{0.1}S (0.1 M CZS), the EDS mapping of (e) Cd, (f)Zn, (g) S and (h) Mo.

results demonstrated that MoS₂ was dispersed on the surface of the Cd_{0.9}Zn_{0.1}S, which was consistent with TEM images [35]. The band gap energy of Cd_{0.9}Zn_{0.1}S and MoS₂ was calculated on the basis of UV-vis absorption spectra through the formula $(ahv)^{m/2} = A(hv - Eg)$. In the formula, the various parameters, a , h , v , A and Eg , are expressed as the absorption coefficient, Plank constant, incident light frequency,

proportionality constant, and band energy, respectively. Since Cd_{0.9}Zn_{0.1}S and MoS₂ was an direct band gap semiconductor, the index m was equal to 1 [34,57]. A plot of $(ahv)^{1/2}$ versus the photo energy (hv) are shown in Fig. 5b. Thus, the band gap energy of Cd_{0.9}Zn_{0.1}S and MoS₂ were calculated on the basis of the intercept of the tangent lines to be 2.30 eV and 2.60 eV, which was similar to previously reported

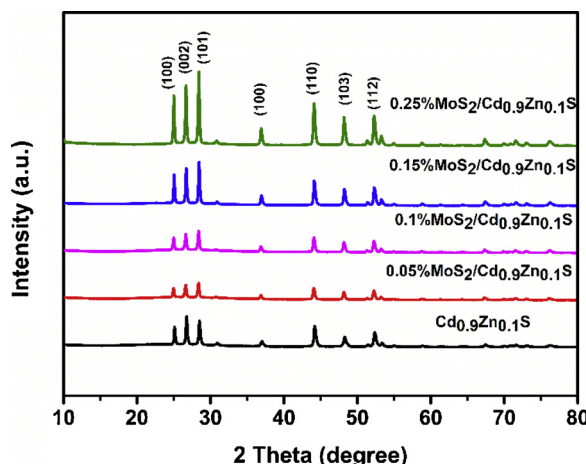


Fig. 2. XRD patterns of 0.1% MoS₂/Cd_{0.9}Zn_{0.1}S composites loaded with different MoS₂ weight ratios.

results [58]. Photoluminescence (PL) analysis was employed to investigate the separation efficiencies of the photoelectrons and holes. A weaker fluorescence emission peak intensity indicated a lower probability that electrons would recombine with holes. The observation in Fig. 6(a) revealed that pure Cd_{0.9}Zn_{0.1}S had an emission band at ~525 nm, which could be attributed to the connatorial band gap emission [59]. It was clear that the PL intensity of 0.1% MoS₂/Cd_{0.9}Zn_{0.1}S was lower than Cd_{0.9}Zn_{0.1}S, which indicated a significant improvement in electron transfer and photocatalytic efficiency due to the introduction of MoS₂ [60]. To further reveal the electron-hole transfer mechanism, the periodic on/off transient photocurrent response experiments were performed. The photocurrent density of 0.1 MCZS composite was about 1.6–2 times as high as that of pure CZS (Fig. 6b), which demonstrated the lower recombination of photoelectrons with holes. The results further revealed that electrons were generated by

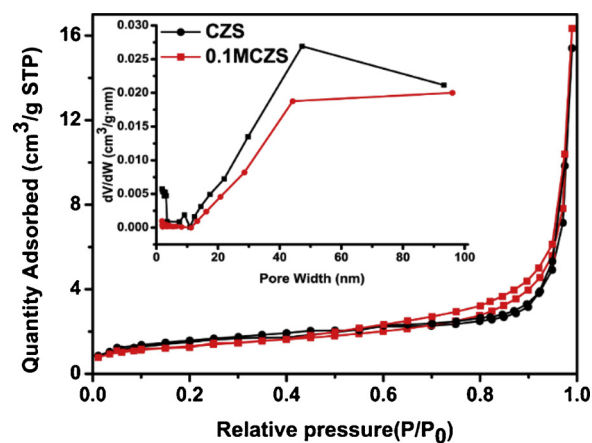


Fig. 4. N₂ adsorption–desorption isotherms, inset: the pore size distribution diagram of Cd_{0.9}Zn_{0.1}S and 0.1%MoS₂/Cd_{0.9}Zn_{0.1}S composites.

photo-excitation transfer to MoS₂, which prevented the recombination of photoelectrons with holes, while improving the photocatalytic efficiency. The electrochemical impedance spectroscopy (EIS) was employed to investigate the transfer ability of charge carriers (Fig. 6c). Obviously, the Nyquist impedance plot of 0.1 MCZS has the smaller arc size in contrast to CZS, which showed that the lower charge-transfer resistance on the electrode surface in 0.1 MCZS composite [61]. It was implied that the introduction of MoS₂ could accelerate the migration speed and separation efficiency of photoinduced charge carriers.

3.4. Photocatalytic performance

The photocatalytic performance of the MoS₂/Cd_{0.9}Zn_{0.1}S samples was evaluated by the degradation of DCF under simulated visible light ($\gamma \geq 420$ nm). Among the different Cd and Zn ratios, the optimal composition was verified to be Cd_{0.9}Zn_{0.1}S, which reflected the highest

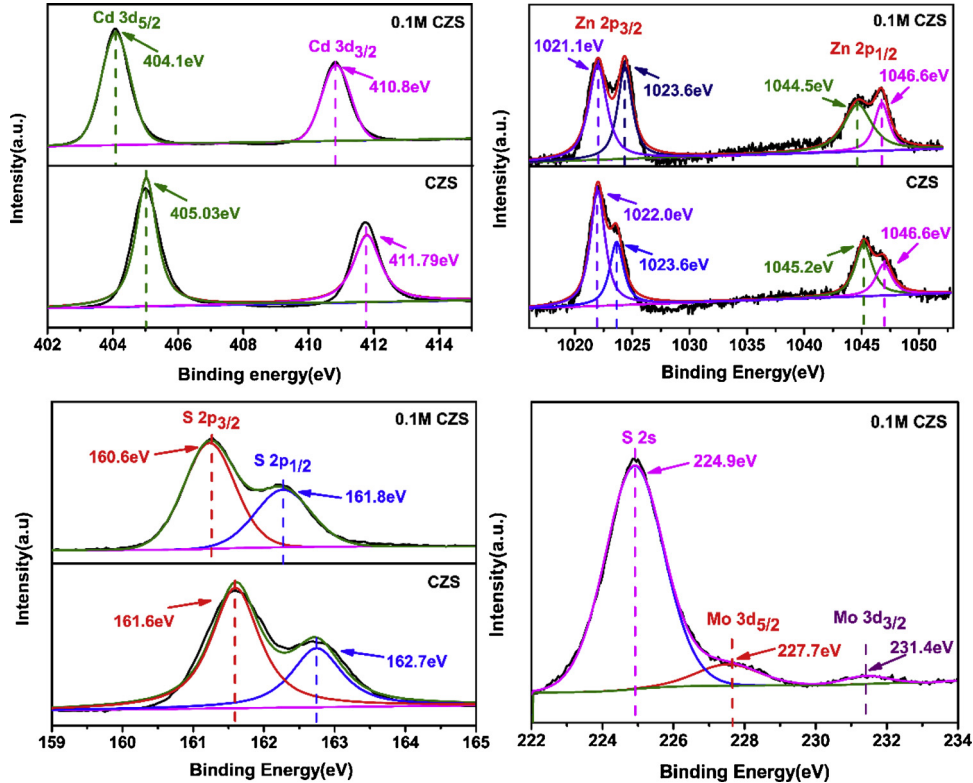


Fig. 3. High-resolution XPS spectra of the 0.1%MoS₂/Cd_{0.9}Zn_{0.1}S composite sample for (a) Cd, (b) Zn, (c) S, and (d) Mo.

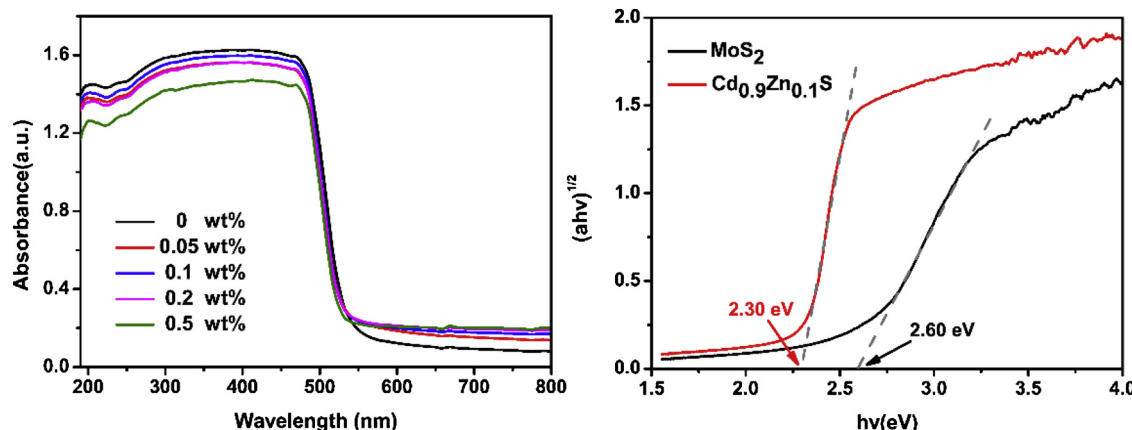


Fig. 5. (a) UV-vis absorption spectra of MoS₂/Cd_{0.9}Zn_{0.1}S composites loaded with different MoS₂ weight ratios (b) plot of $(ahv)^{1/2}$ versus the photo energy ($h\nu$) for Cd_{0.9}Zn_{0.1}S and 0.1% MoS₂/Cd_{0.9}Zn_{0.1}S.

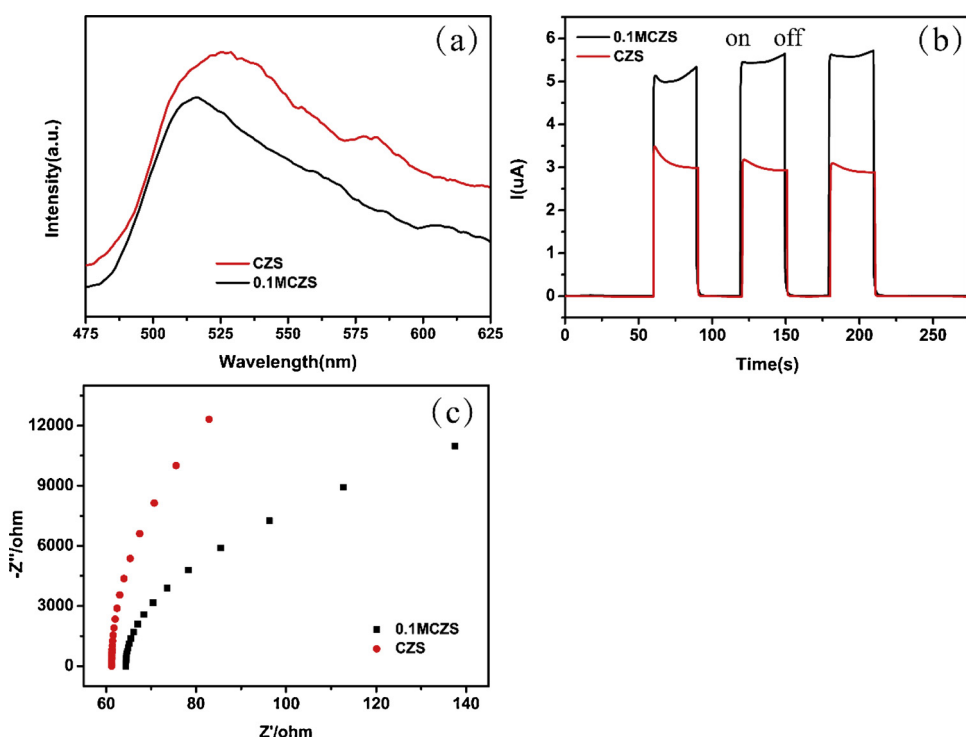


Fig. 6. (a) Photoluminescence (PL) emission spectra (b) Transient photocurrent density responses and (c) EIS Nyquist plots of Cd_{0.9}Zn_{0.1}S and 0.1%MoS₂/Cd_{0.9}Zn_{0.1}S.

degradation efficiency between Cd_xZn_{1-x}S ($x = 0.1, 0.4, 0.6, 0.8, 0.9$) (Fig. S2). Meanwhile, the actual atomic ratio of Cd²⁺: Zn²⁺ in the samples were tested by ICP-OES (Table S4). Pristine Cd_{0.9}Zn_{0.1}S showed some photocatalytic performance; however, the DCF degradation rate was low (58%) due to its poor separation ability (Fig. 7a). Following the introduction of MoS₂, the DCF degradation rate gradually increased. The photocatalytic activity of MoS₂/Cd_{0.9}Zn_{0.1}S increased with higher MoS₂ content, from 0 wt% to 0.1 wt%. A further increase in MoS₂ (> 0.1 wt%) resulted in a reduction in the DCF degradation rates, which may have been due to the blockage of active sites with the excess MoS₂ [46]. These results implied that higher DCF degradation efficiencies were contingent on optimal MoS₂ loading. And the actual loading content x wt% of MoS₂ on Cd_{0.9}Zn_{0.1}S in samples ($x = 0.05, 0.1, 0.15, 0.25$) were measured via the ICP-OES (Table S5). The effects of the catalyst concentration on the DCF degradation rate under the visible light catalytic system are shown in Fig. 7b. The removal rate increased with the increase of photocatalyst dosage, from 0.25 g/L to 1.00 g/L, which was attributed to the emergence of additional active

species. Furthermore, the increased photocatalyst concentration induced the trapped photoelectrons to accelerate the generation of reactive species. The effects of different initial pH were also investigated for the degradation of DCF. As illustrated in Fig. 7c, the residual DCF concentration decreased gradually as the pH was elevated, in the range of from 4 to 11 (Fig. 6c). The zero potential of 0.1% MoS₂/Cd_{0.9}Zn_{0.1}S was 2.24 (Fig. S3), which indicated that the photocatalyst surface remained negative at pH > 2.24. At more acidic pH values (pH < 4.15), an attractive force emerged between the protonated DCF (pKa = 4.15) [62] and the negative photocatalyst surface, leading to a remarkable degradation rate. Thereafter, with further elevated pH (pH > 4.15), most of the DCF was presented as anionic species, and the degree of dissociation increased gradually. At pH 11, the repulsion interaction between the DCF and 0.1 M SZC became stronger due to the complete dissociation of DCF, which hindered its removal efficiency. To evaluate the potential for the photocatalyst in practical application, the stability and recyclability of the 0.1%MoS₂/Cd_{0.9}Zn_{0.1}S composite were investigated by cycling performances for the degradation of DCF under

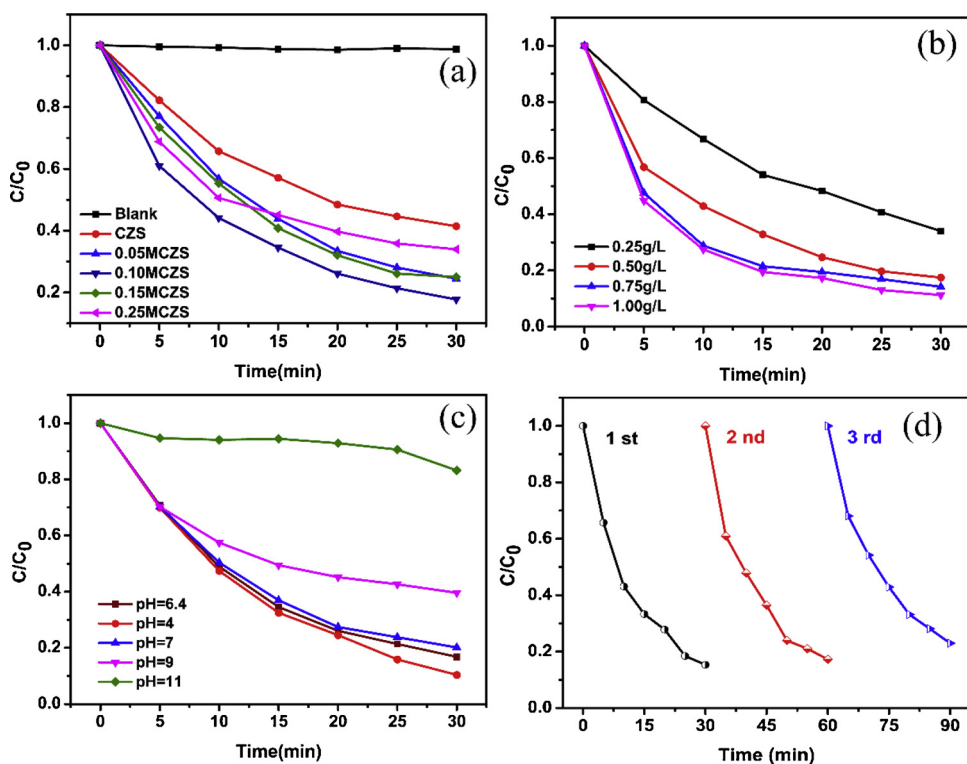


Fig. 7. (a) Photocatalytic degradation of DCF in the presence of Cd_{0.9}Zn_{0.1}S and the different MoS₂ loading proportions; effect of various factors on the degradation of DCF: (b) dosage of 0.1 M CZS catalyst (c) different initial pH. (d) Cycle runs of the photocatalytic degradation activities over the 0.1 MCZS photocatalyst.

the same conditions. There was no significant reduction in the photocatalytic degradation performance even after three cycles (Fig. 7d). The result revealed that photocatalytic DCF degradation of 0.1 wt% MoS₂/Cd_{0.9}Zn_{0.1}S photocatalyst exhibited excellent stability and reusability.

3.5. Photocatalytic mechanisms

To elucidate the photocatalytic mechanism, the primary reactive radicals in the MoS₂/Cd_{0.9}Zn_{0.1}S/Vis system were detected through quenching experiments (Fig. 8a). Quenching agents (e.g., isopropanol (IPA, 100 mM), benzoquinone (BQ, 1 mM), and sodium oxalate (Na₂C₂O₄, 10 mM)) were employed as hydroxyl radical (·OH), superoxide (O₂^{·-}), and hole (h⁺) scavengers [63]. It may be seen clearly from Fig. 8a that the DCF removal rate decreased by 4%, 67%, and 41%, which were attributed to ·OH, O₂^{·-}, and h⁺, respectively. From Fig. 8a, it is evident that ·OH had a negligible impact, while h⁺ (which was generated in the valence band) played a key function in the DCF degradation process through direct electron transfer. Further, the vital role of O₂^{·-} throughout the DCF elimination process could not be ignored. Electron spin resonance (ESR) was performed to identify the reactive species. As depicted in Fig. 8, the intensity trends for DMPO-O₂^{·-} and DMPO-OH adducts were conducted in the dark and under visible light irradiation for 5 min and 10 min. The intensity of DMPO-O₂^{·-} adducts in the 0.1 M CZS materials were stronger than the pure CZS, while there was no O₂^{·-} signal in the dark (Fig. 8b). The CZS hybridized with MoS₂ demonstrated a much higher DMPO-OH adduct intensity than pure CZS (Fig. 8c). The 0.1 M CZS compounds generated more O₂^{·-} and ·OH, which translated to a higher oxidation capacity and DCF degradation rate [64].

3.6. Transformation pathway and mineralization

Total organic carbon (TOC) removal was employed to assess the mineralization of DCF (Fig. 9). The DCF degradation rate attained 84% when the light exposure time was 30 min; however, only 30% of the

TOC was removed. This signified that DCF may be decomposed to other relatively stable substances. When the light exposure time was extended to 60 min, 65% of the TOC was eliminated, which demonstrated that DCF could be expected to undergo complete mineralization over a longer period of time. Potential intermediates were detected through HRAM LC/MS/MS, and the following DCF degradation pathways were proposed accordingly. Three pathways were involved in the photocatalytic system based on the structural elucidation of nine intermediates (Fig. 10). The retention time, m/z ratios, and supposed structure are summarized in Table S5, with the secondary ion mass spectrum in Fig. S4(a-f). According to previous research [65], the C3 atom on the DCF with the highest electron cloud density would be attacked by the electrophilic ·OH, therefore yielding a monohydric DCF derivative compound (m/z 311). Hydroxylation elevated the electron cloud density on the benzene ring, which was more conducive to electrophilic species attack, leading to the loss of chlorine and the production of multi-hydroxylated compounds (m/z 293) [66-68]. Subsequently, the bridge between the aromatic rings was broken by h⁺ attack [69], with the development of small-molecule products (m/z 144, 151). On the one hand, C4 with the low electron densities were easily oxidized by nucleophilic O₂^{·-} to form a zwitterion or diradical, which was further generated the m/z 327 [70]. Subsequently, by-products (m/z 151, 179) were produced via the cleavage of C-N bond cleavage [65]. On the other hand, O₂^{·-} could assault the C15 position to generate intermediate on account of its nucleophilic character [71]. The phenylacetic acid group on the diradical was directly oxidized to an aldehyde group (m/z 229) [70]. And the transition state product (m/z 229) was further attacked by electrophilic ·OH to generate m/z 122. Finally, the intermediates were mineralized to CO₂, H₂O, NH₄⁺, and Cl⁻. Based on the above results, the reaction mechanism of MoS₂/Cd_{0.9}Zn_{0.1}S under visible light irradiation for the degradation of DCF was proposed, as shown in Fig. 11. The band gap energy (Eg) of Cd_{0.9}Zn_{0.1}S and MoS₂ were calculated to be 2.30 eV and 2.60 eV by Tauc's plot, respectively (Fig. 5b). Their corresponding flat band potentials were directly measured by a Mott-Schottky plot, and the VB

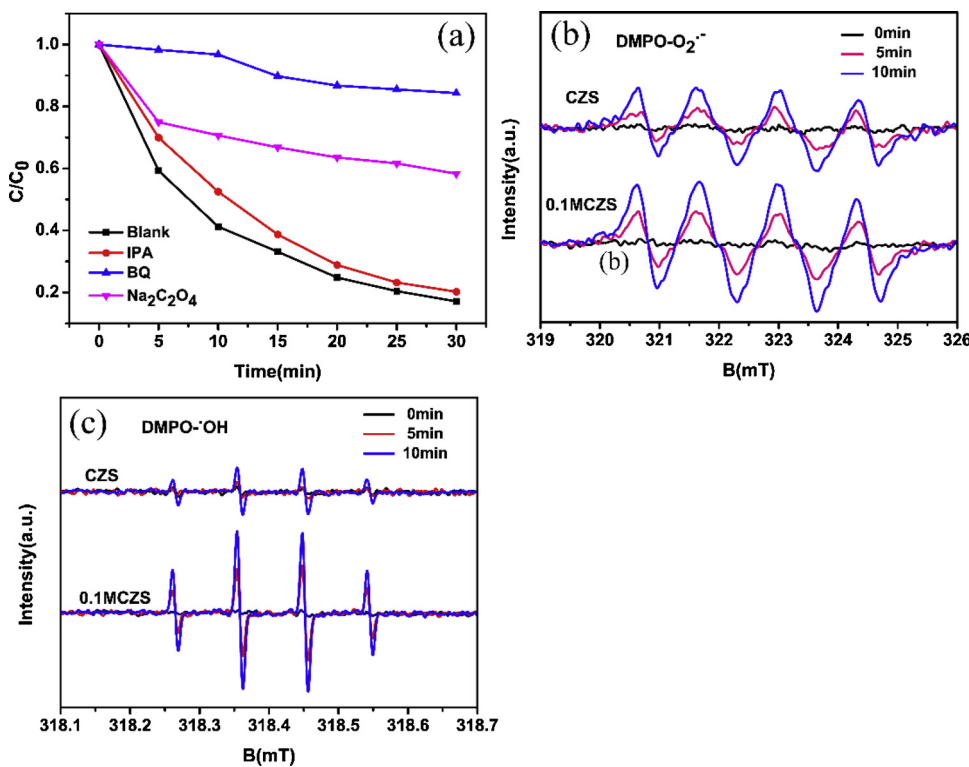


Fig. 8. (a) Relevant species quenching experiments (b) ESR spectra of DMPO-O₂⁻ and (c) DMPO-OH signals recorded with pure Cd_{0.9}Zn_{0.1}S and 0.1%MoS₂/Cd_{0.9}Zn_{0.1}S.

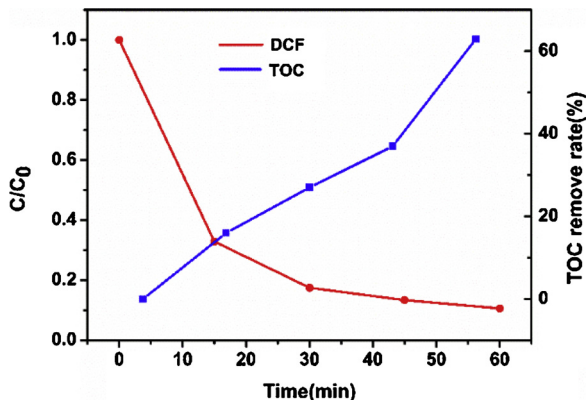


Fig. 9. The mineralization of DCF during the 0.1% MoS₂/Cd_{0.9}Zn_{0.1}S photo-catalytic degradation process.

positions were determined combined with the previously obtained band gap (Fig. S5). Previous research has revealed that the flat band potentials of n-type semiconductors equal the conduction band [72]. The relative conduction band (CB) of the Cd_{0.9}Zn_{0.1}S and MoS₂ was estimated to be -0.50 eV and -0.35 eV, respectively, versus the normal hydrogen electrode (NHE). Hence, on the basis of formula $E_{VB} = E_g - E_{CB}$, the valence bands (VB) of the Cd_{0.9}Zn_{0.1}S and MoS₂ were calculated to be 1.80 eV and 2.25 eV, respectively. According to the above calculations, the energy level mechanism diagram of Cd_{0.9}Zn_{0.1}S/MoS₂ was shown in Fig. 10. Under visible light irradiation, Cd_{0.9}Zn_{0.1}S/MoS₂ compounds could produce rich photogenerated electrons (e^-) and holes (h^+) (Eq. (1)). The photoinduced electrons in Cd_{0.9}Zn_{0.1}S could easily transfer to the CB of MoS₂ because of the more negative CB of Cd_{0.9}Zn_{0.1}S. Meanwhile, the holes in the MoS₂ valence band (VB) would be injected into the VB of Cd_{0.9}Zn_{0.1}S. The electron/hole recombination rate was greatly decreased, whereas the core-shell Cd_{0.9}Zn_{0.1}S and MoS₂ heterostructure provided a convenient transfer channel for more

free electrons to accumulate in the conduction band. More importantly, the CB of MoS₂ (-0.35 eV) was negative than the E₀ (O₂/O₂⁻) (-0.33 eV) [73], which meant that the electrons could react with O₂ to form O₂⁻ (Eq. (2)). Further, the production pathway of OH may be expounded according to the following equation (Eqs. (3 and 4)) [74]. To sum up, h⁺, O₂⁻ and OH provided great contribution to the degradation of DCF in the Cd_{0.9}Zn_{0.1}S/MoS₂/Vis system.



4. Conclusions

Heterostructured high efficient core-shell photocatalysts MoS₂/Cd_{0.9}Zn_{0.1}S was successfully synthesized. A series of experiments and characterizations clearly showed that the photocatalytic properties of 0.1% MoS₂/Cd_{0.9}Zn_{0.1}S was significantly greater than pristine Cd_{0.9}Zn_{0.1}S for the degradation of diclofenac (DCF). The loading of MoS₂ co-catalyst onto Cd_{0.9}Zn_{0.1}S improved the photoelectron-hole separation efficiency as well as enhanced the photocatalytic activity. More importantly, it provided additional active sites to facilitate the formation of reactive superoxide radical (O₂⁻) and hole (h⁺) species. Hydroxylation, dechloridation, and oxidization to aldehyde were discovered to be the major pathways responsible for the degradation of DCF. It is hoped that our work may advance the feasible application of sulfide semiconductor photocatalysts for the efficient degradation of organic pollutants.

Declaration of Competing Interest

The authors declare that they have no known competing financial

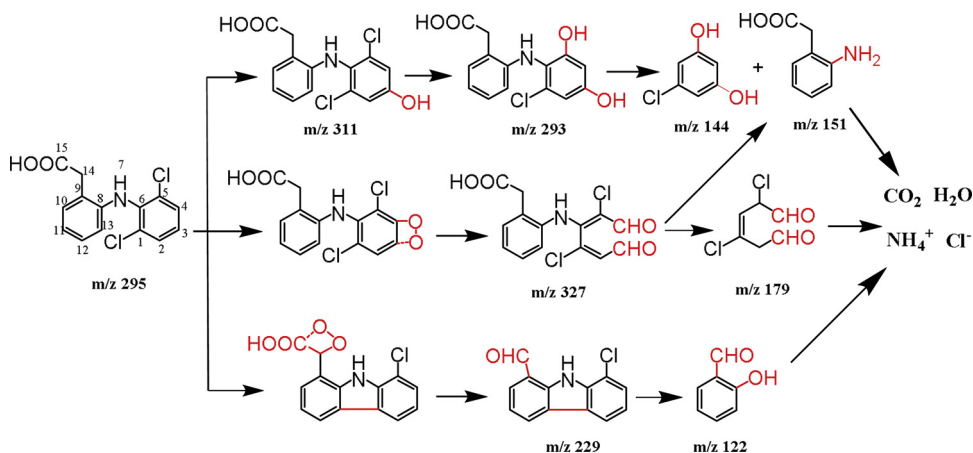


Fig. 10. Potential DCF degradation pathways in 0.1% MoS₂/Cd_{0.9}Zn_{0.1}S under visible light irradiation.

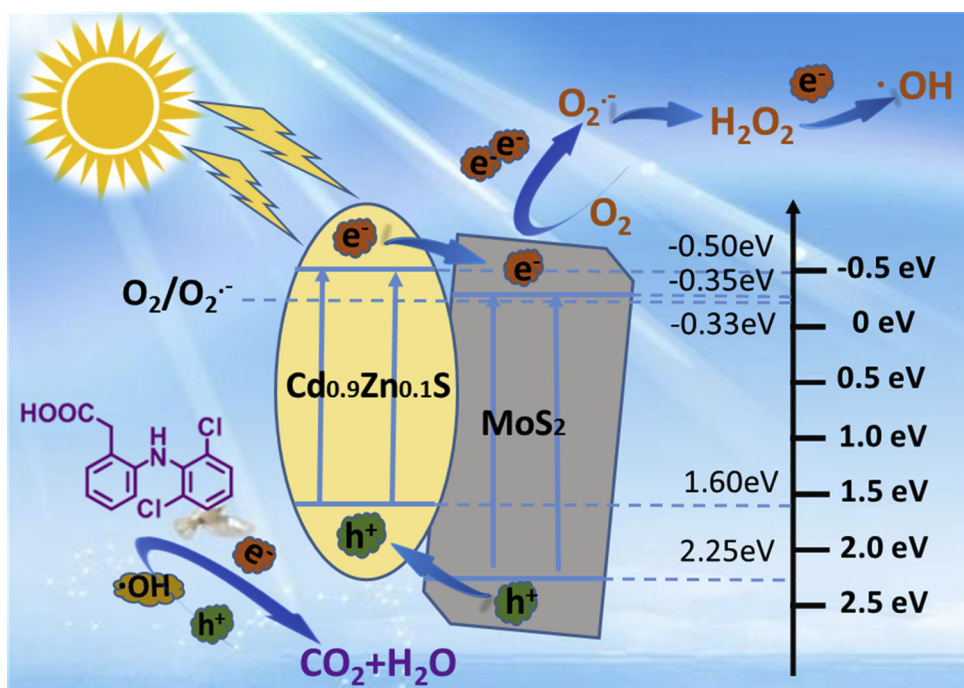


Fig. 11. Diagram of DCF degradation mechanism by MoS₂/Cd_{0.9}Zn_{0.1}S photocatalyst under visible light.

interests or personal relationships that could have appeared to influence the work reported in this paper.

Acknowledgment

This work was supported by the National Natural Science Foundation, China, Guoguang Liu [No. 21677040 and 21377031], the National Science and Technology plan Project, China, Wenyang Lv [2018-281], Guangdong Provincial Science and the Technology Plan Project, China, Wenyang Lv [No. 2017A020216010], Guangzhou City Science and the Technology Plan Project, China, Guoguang Liu [No. 201903010080].

Appendix A. Supplementary data

Supplementary material related to this article can be found, in the online version, at doi:<https://doi.org/10.1016/j.apcatb.2019.118033>.

References

- [1] J.L. Liu, M.H. Wong, Pharmaceuticals and personal care products (PPCPs): a review on environmental contamination in China, Environ. Int. 59 (2013) 208–224, <https://doi.org/10.1016/j.envint.2013.06.012>.
- [2] Y. Wang, H. Liu, G. Liu, Y. Xie, S. Gao, Oxidation of diclofenac by potassium ferrate (VI): Reaction kinetics and toxicity evaluation, Sci. Total Environ. 506–507 (2015) 252–258, <https://doi.org/10.1016/j.scitotenv.2014.10.114>.
- [3] Z. Wei, Z. Li, H. Deng, Ag modified g-C₃N₄ composites with enhanced visible-light photocatalytic activity for diclofenac degradation, J. Mol. Catal. A Chem. 423 (2016) 270–276, <https://doi.org/10.1016/j.molcata.2016.07.021>.
- [4] Y. Wang, H. Liu, G. Liu, Y. Xie, Oxidation of diclofenac by aqueous chlorine dioxide: identification of major disinfection byproducts and toxicity evaluation, Sci. Total Environ. 473–474 (2014) 437–445, <https://doi.org/10.1016/j.scitotenv.2013.12.056>.
- [5] S. Suárez, M. Carballa, F. Omil, J.M. Lema, How are pharmaceutical and personal care products (PPCPs) removed from urban wastewaters, Chemosphere 40 (2009) 125–138, <https://doi.org/10.1002/chin.200919268>.
- [6] S. Myint, Z. Marco, T. Jochen, T.C. Schmidt, G. Alfred, V.S. Clemens, Oxidation of diclofenac with ozone in aqueous solution, Environ. Sci. Technol. 42 (2008) 6656–6662, <https://doi.org/10.1021/es0808612>.
- [7] J. Hofmann, U. Freier, M. Wecks, S. Hohmann, Degradation of diclofenac in water by heterogeneous catalytic oxidation with H₂O₂, Appl. Catal. B 70 (2007) 447–451, <https://doi.org/10.1016/j.apcatb.2005.11.023>.
- [8] D. Vogna, R. Marotta, A. Napolitano, R. Andreozzi, M. d'Ischia, Advanced oxidation

of the pharmaceutical drug diclofenac with UV/H₂O₂ and ozone, *Water Res.* 38 (2004) 414–422, <https://doi.org/10.1016/j.watres.2003.09.028>.

[9] B. Czech, K. Rubinowska, TiO₂-assisted photocatalytic degradation of diclofenac, metoprolol, estrone and chloramphenicol as endocrine disruptors in water, *Adsorption* 19 (2013) 619–630, <https://doi.org/10.1007/s10450-013-9485-8>.

[10] V.C. Saradisid, K.V. Plakas, S.I. Patsios, A.J. Karabelas, Investigation of diclofenac degradation in a continuous photo-catalytic membrane reactor. Influence of operating parameters, *Chem. Eng. J.* 239 (2014) 299–311, <https://doi.org/10.1016/j.cej.2013.11.026>.

[11] W.C. Peng, X.Y. Li, Synthesis of MoS₂/g-C₃N₄ as a solar light-responsive photocatalyst for organic degradation, *Catal. Commun.* 49 (2014) 63–67, <https://doi.org/10.1016/j.catcom.2014.02.008>.

[12] Y. Bessekhouad, D. Robert, J.V. Weber, Bi₂S₃/TiO₂ and CdS/TiO₂ heterojunctions as an available configuration for photocatalytic degradation of organic pollutant, *J. Photochem. Photobiol. A: Chem.* 163 (2004) 569–580, <https://doi.org/10.1016/j.jphotochem.2004.02.006>.

[13] L. Suhadolnik, A. Pohar, B. Likozar, M. Čeh, Mechanism and kinetics of phenol photocatalytic, electrocatalytic and photoelectrocatalytic degradation in a TiO₂-nanotube fixed-bed microreactor, *Chem. Eng. J.* 303 (2016) 292–301, <https://doi.org/10.1016/j.cej.2016.06.027>.

[14] M. Krivec, A. Pohar, B. Likozar, G. Dražić, Hydrodynamics, mass transfer, and photocatalytic phenol selective oxidation reaction kinetics in a fixed TiO₂ micro-reactor, *Aiche J.* 61 (2015) 572–581, <https://doi.org/10.1002/aic.14648>.

[15] L. Suhadolnik, A. Pohar, U. Novak, B. Likozar, A. Mihelič, M. Čeh, Continuous photocatalytic, electrocatalytic and photo-electrocatalytic degradation of a reactive textile dye for wastewater-treatment processes: batch, microreactor and scaled-up operation, *J. Ind. Eng. Chem.* 72 (2019) 178–188, <https://doi.org/10.1016/j.jiec.2018.12.017>.

[16] Y. Bessekhouad, D. Robert, J.V. Weber, Bi₂S₃/TiO₂ and CdS/TiO₂ heterojunctions as an available configuration for photocatalytic degradation of organic pollutant, *J. Photochem. Photobiol. A: Chem.* 163 (2004) 569–580, <https://doi.org/10.1016/j.jphotochem.2004.02.006>.

[17] P.K.J. Robertson, Semiconductor photocatalysis: an environmentally acceptable alternative production technique and effluent treatment process, *J. Clean. Prod.* 4 (2016) 203–212, [https://doi.org/10.1016/s0959-6526\(96\)00044-3](https://doi.org/10.1016/s0959-6526(96)00044-3).

[18] C. Zhu, C. Liu, Y. Zhou, Y. Fu, S. Guo, H. Li, S. Zhao, H. Huang, Y. Liu, Z. Kang, Carbon dots enhance the stability of CdS for visible-light-driven overall water splitting, *Appl. Catal. B* 216 (2017) 114–121, <https://doi.org/10.1016/j.apcatb.2017.05.049>.

[19] N. Qin, J. Xiong, R. Liang, Y. Liu, S. Zhang, Y. Li, Z. Li, L. Wu, Highly efficient photocatalytic H₂ evolution over MoS₂/CdS-TiO₂ nanofibers prepared by an electrospinning mediated photodeposition method, *Appl. Catal. B* 202 (2017) 374–380, <https://doi.org/10.1016/j.apcatb.2016.09.040>.

[20] D.P. Kumar, S. Hong, D.A. Reddy, T.K. Kim, Noble metal-free ultrathin MoS₂ nanosheet-decorated CdS nanorods as an efficient photocatalyst for spectacular hydrogen evolution under solar light irradiation, *J. Mater. Chem. A* 4 (2016) 18551–18558, <https://doi.org/10.1039/C6TA08628D>.

[21] S. Ma, J. Xie, J. Wen, K. He, X. Li, W. Liu, X. Zhang, Constructing 2D layered hybrid CdS nanosheets/MoS₂ heterojunctions for enhanced visible-light photocatalytic H₂ generation, *Appl. Surf. Sci.* 391 (2017) 580–591, <https://doi.org/10.1016/j.apsusc.2016.07.067>.

[22] W. Yao, X. Song, C. Huang, Q. Xu, Q. Wu, Enhancing solar hydrogen production via modified photochemical treatment of Pt/CdS photocatalyst, *Catal. Today* 199 (2013) 42–47, <https://doi.org/10.1016/j.cattod.2012.05.003>.

[23] J. Feng, C. An, L. Dai, J. Liu, G. Wei, S. Bai, J. Zhang, Y. Xiong, Long-term production of H₂ over Pt/CdS nanoplates under sunlight illumination, *Chem. Eng. J.* 283 (2016) 351–357, <https://doi.org/10.1016/j.cej.2015.07.079>.

[24] Y. Shi, H. Li, L. Wang, W. Shen, H. Chen, Novel α-Fe₂O₃/CdS cornlike nanorods with enhanced photocatalytic performance, *ACS Appl. Mater. Interfaces* 4 (2012) 4800–4806, <https://doi.org/10.1021/am3011516>.

[25] X. Wei, J. Pan, S. Wang, J. Mei, Y. Zheng, C. Cui, C. Li, CdS modified Cu₂O octahedral nano-heterojunction and its photocatalytic application, *J. Mater. Sci. Mater. Electron.* 18 (2017) 14079–14084, <https://doi.org/10.1007/s10854-017-7259-x>.

[26] E. Busby, A. Thibert, L.E. Page, A.M. Jawaid, P.T. Snee, D.S. Larsen, Primary charge carrier dynamics of water-solubilized CdZnS/ZnS core/shell and CdZnS/ZnS-Pd nanoparticle adducts, *Chem. Phys. Lett.* 573 (2013) 56–62, <https://doi.org/10.1016/j.cplett.2013.04.045>.

[27] D. Rodic, V. Spasojevic, A. Bajorek, P. Onnerud, Similarity of structure properties of Hg_{1-x}Mn_xS and Cd_{1-x}Mn_xS (structure properties of HgMnS and CdMnS), *J. Magn. Magn. Mater.* 152 (1996) 159–164, [https://doi.org/10.1016/0304-8853\(95\)00435-1](https://doi.org/10.1016/0304-8853(95)00435-1).

[28] A.H. Reshak, Novel photocatalytic water splitting solar-to-hydrogen energy conversion: CdLa₂S₄ and CdLa₂Se₄ ternary semiconductor compounds, *J. Chem. Soc. Faraday Trans. 2* 20 (2018) 8848–8858, <https://doi.org/10.1039/C8CP00373D>.

[29] M. Kimi, L. Yuliati, M. Shamsuddin, Photocatalytic hydrogen production under visible light over Cd_{0.1}Sn_xZn_{0.9-x}S solid solution photocatalysts, *Int. J. Hydrogen Energy* 36 (2011) 9453–9461, <https://doi.org/10.1016/j.ijhydene.2011.05.044>.

[30] Y. Zhou, Y. Wang, T. Wen, S. Zhang, B. Chang, Y. Guo, B. Yang, Mesoporous Cd_{1-x}Zn_xS microspheres with tunable bandgap and high specific surface areas for enhanced visible-light-driven hydrogen generation, *J. Colloid Interface Sci.* 467 (2016) 97–104, <https://doi.org/10.1016/j.jcis.2016.01.003>.

[31] W. Li, D. Li, Z. Chen, H. Huang, M. Sun, Y. He, X. Fu, High-efficient degradation of dyes by Zn_xCd_{1-x}S solid solutions under visible light irradiation, *J.phys.chem.c* 112 (2008) 14943–14947, <https://doi.org/10.1021/jp0849075>.

[32] L. Ye, C. Han, Z. Ma, Y. Leng, J. Li, X. Ji, D. Bi, H. Xie, Z. Huang, Ni₂P loading on Cd_{0.5}Zn_{0.5}S solid solution for exceptional photocatalytic nitrogen fixation under visible light, *Chem. Eng. J.* 307 (2017) 311–318, <https://doi.org/10.1016/j.cej.2016.08.102>.

[33] D. Li, Z. Wu, C. Xing, D. Jiang, M. Chen, W. Shi, S. Yuan, Novel Zn_{0.8}Cd_{0.2}S/g-C₃N₄ heterojunctions with superior visible-light photocatalytic activity: Hydrothermal synthesis and mechanism study, *J. Mol. Catal. A Chem.* 395 (2014) 261–268, <https://doi.org/10.1016/j.molcata.2014.08.036>.

[34] B. Han, S. Liu, N. Zhang, Y.J. Xu, Z.R. Tang, One-dimensional CdS@MoS₂ core-shell nanowires for boosted photocatalytic hydrogen evolution under visible light, *Appl. Catal. B* 202 (2017) 298–304, <https://doi.org/10.1016/j.apcatb.2016.09.023>.

[35] J. Xu, X. Cao, Characterization and mechanism of MoS₂/CdS composite photocatalyst used for hydrogen production from water splitting under visible light, *Chem. Eng. J.* 260 (2015) 642–648, <https://doi.org/10.1016/j.cej.2014.07.046>.

[36] Y. Min, G. He, Q. Xu, Y. Chen, Dual-functional MoS₂ sheet-modified CdS branch-like heterostructures with enhanced photostability and photocatalytic activity, *J. Mater. Chem. A* 2 (2014) 2578–2584, <https://doi.org/10.1039/C3TA14240J>.

[37] Z. Wang, B. Mi, Environmental applications of 2D molybdenum disulfide (MoS₂) nanosheets, *Environ. Sci. Technol.* 51 (2017) 8229–8244, <https://doi.org/10.1021/acs.est.7b01466>.

[38] W. Zhang, X. Xiao, L. Zheng, C. Wan, Fabrication of TiO₂/MoS₂ composite photocatalyst and its photocatalytic mechanism for degradation of methyl orange under visible light, *Can. J. Chem. Eng.* 93 (2015) 1594–1602, <https://doi.org/10.1002/cjce.22245>.

[39] I.F. Ertis, I. Boz, Synthesis and characterisation of MoS₂-CdS catalyst for photocatalytic degradation of methylene blue from aqueous solution, *J. Chem. Res.* 41 (2017) 529–533, <https://doi.org/10.3184/174751917X15027989009017>.

[40] X. Lu, Y. Wang, X. Zhang, G. Xu, D. Wang, J. Lv, Z. Zheng, Y. Wu, NiS and MoS₂ nanosheet co-modified graphitic C₃N₄ ternary heterostructure for high efficient visible light photodegradation of antibiotic, *J. Hazard. Mater.* 341 (2017) 10–19, <https://doi.org/10.1016/j.jhazmat.2017.07.004>.

[41] X. Wang, J. Chen, X. Guan, L. Guo, Enhanced efficiency and stability for visible light driven water splitting hydrogen production over Cd_{0.5}Zn_{0.5}S/g-C₃N₄ composite photocatalyst, *Int. J. Hydrogen Energy* 40 (2015) 7546–7552, <https://doi.org/10.1016/j.ijhydene.2014.11.055>.

[42] T. Fotiou, T.M. Triantis, T. Kaloudis, K.E. O'Shea, D.D. Dionysiou, A. Hiskia, Assessment of the roles of reactive oxygen species in the UV and visible light photocatalytic degradation of cyanotoxins and water taste and odor compounds using C-TiO₂, *Water Res.* 90 (2016) 52–61, <https://doi.org/10.1016/j.watres.2015.12.006>.

[43] G. Li, X. Nie, Y. Gao, T. An, Can environmental pharmaceuticals be photocatalytically degraded and completely mineralized in water using g-C₃N₄/TiO₂ under visible light irradiation—implications of persistent toxic intermediates, *Appl. Catal. B* 180 (2016) 726–732, <https://doi.org/10.1016/j.apcatb.2015.07.014>.

[44] F. Xue, W. Fu, M. Liu, X. Wang, B. Wang, L. Guo, Insight into Cd_{0.9}Zn_{0.1}S solid-solution nanotetrapods: Growth mechanism and their application for photocatalytic hydrogen production, *Int. J. Hydrogen Energy* 41 (2016) 20455–20464, <https://doi.org/10.1016/j.ijhydene.2016.07.233>.

[45] Q.-Z. Huang, Y. Xiong, Q. Zhang, H.-C. Yao, Z.-J. Li, Noble metal-free MoS₂ modified Mn_{0.25}Cd_{0.75}S for highly efficient visible-light driven photocatalytic H₂ evolution, *Appl. Catal. B* 209 (2017) 514–522, <https://doi.org/10.1016/j.apcatb.2017.03.035>.

[46] Q.Z. Huang, Y. Xiong, Q. Zhang, H.C. Yao, Z.J. Li, Noble metal-free MoS₂ modified Mn_{0.25}Cd_{0.75}S for highly efficient visible-light driven photocatalytic H₂ evolution, *Appl. Catal. B* 209 (2017) 514–522, <https://doi.org/10.1016/j.apcatb.2017.03.035>.

[47] Z. Yan, L. Du, D.L. Phillips, Multilayer core-shell MoS₂/CdS nanorods with very high photocatalytic activity for hydrogen production under visible-light excitation and investigation of the photocatalytic mechanism by femtosecond transient absorption spectroscopy, *RSC Adv.* 7 (2017) 55993–55999, <https://doi.org/10.1039/C7RA12118K>.

[48] Q. Li, H. Meng, P. Zhou, Y. Zheng, J. Wang, J. Yu, J.R. Gong, Zn_{1-x}Cd_xS solid solutions with controlled Bandgap and enhanced visible-light photocatalytic H₂-production activity, *ACS Catal.* 3 (2013) 882–889, <https://doi.org/10.1021/cs4000975>.

[49] C. Zamfirescu, I. Dincer, G.F. Naterer, R. Banica, Quantum efficiency modeling and system scaling-up analysis of water splitting with Cd_{1-x}Zn_xS solid-solution photocatalyst, *Chem. Eng. Sci.* 97 (2013) 235–255, <https://doi.org/10.1016/j.ces.2013.04.020>.

[50] P. Niu, L. Zhang, G. Liu, H.M. Cheng, Graphene-like carbon nitride nanosheets for improved photocatalytic activities, *Adv. Funct. Mater.* 22 (2012) 4763–4770, <https://doi.org/10.1002/adfm.201200922>.

[51] L. Yao, D. Wei, Y. Ni, D. Yan, C. Hu, Surface localization of CdZnS quantum dots onto 2D g-C₃N₄ ultrathin microribbons: Highly efficient visible light-induced H₂-generation, *Nano Energy* 26 (2016) 248–256, <https://doi.org/10.1016/j.nanoen.2016.05.031>.

[52] M. Dan, Q. Zhang, S. Yu, A. Prakash, Y. Lin, Y. Zhou, Noble-metal-free MnS/In₂S₃ composite as highly efficient visible light driven photocatalyst for H₂ production from H₂S, *Appl. Catal. B* 217 (2017) 530–539, <https://doi.org/10.1016/j.apcatb.2017.06.019>.

[53] L. Wei, Y. Chen, Y. Lin, H. Wu, R. Yuan, Z. Li, MoS₂ as non-noble-metal co-catalyst for photocatalytic hydrogen evolution over hexagonal ZnIn₂S₄ under visible light irradiations, *Appl. Catal. B* 144 (2014) 521–527, <https://doi.org/10.1016/j.apcatb.2013.07.064>.

[54] A. Wu, C. Tian, Y. Jiao, Q. Yan, G. Yang, H. Fu, Sequential two-step hydrothermal growth of MoS₂/CdS core-shell heterojunctions for efficient visible light-driven photocatalytic H₂ evolution, *Appl. Catal. B* 203 (2016) 955–963, <https://doi.org/10.1016/j.apcatb.2016.11.009>.

[55] S. Peng, A. Ran, Y. Li, G. Lu, S. Li, Remarkable enhancement of photocatalytic

hydrogen evolution over Cd_{0.5}Zn_{0.5}S by bismuth-doping, Int. J. Hydrogen Energy 37 (2012) 1366–1374, <https://doi.org/10.1016/j.ijhydene.2011.09.140>.

[56] Y.J. Yuan, D. Chen, J. Zhong, L.X. Yang, J.J. Wang, M. Liu, Z.T. Yu, W. Tu, Z. Zou, Interface engineering of noble-metal-free 2D-2D MoS₂/Cu-ZnIn₂S₄ photocatalyst for enhanced photocatalytic H₂ production, J. Mater. Chem. A 5 (2017) 15771, <https://doi.org/10.1039/C7TA04410K>.

[57] Z. Cheng, C. Liu, Y. Zhou, Y. Fu, S. Guo, L. Hao, S. Zhao, H. Hui, L. Yang, Z. Kang, Carbon dots enhance the stability of CdS for visible-light-driven overall water splitting, Appl. Catal. B 216 (2017) 114–121, <https://doi.org/10.1016/j.apcatb.2017.05.049>.

[58] C. Zamfirescu, I. Dincer, G.F. Naterer, R. Banica, Quantum efficiency modeling and system scaling-up analysis of water splitting with Cd_{1-x}Zn_xS solid-solution photocatalyst, Chem. Eng. Sci. 97 (2013) 235–255, <https://doi.org/10.1016/j.ces.2013.04.020>.

[59] Z. Qin, F. Xue, Y. Chen, S. Shen, L. Guo, Spatial charge separation of one-dimensional Ni₂P-Cd_{0.9}Zn_{0.1}S/g-C₃N₄ heterostructure for high-quantum-yield photocatalytic hydrogen production, Appl. Catal. B 217 (2017) 551–559, <https://doi.org/10.1016/j.apcatb.2017.06.018>.

[60] D.A. Reddy, H. Park, R. Ma, D.P. Kumar, M. Lim, T.K. Kim, Heterostructured WS₂-MoS₂ ultrathin nanosheets integrated on CdS nanorods to promote charge separation and migration and improve solar-driven photocatalytic hydrogen evolution, Chemsuschem 10 (2017) 1563, <https://doi.org/10.1002/cssc.201601799>.

[61] W. Xu, C. Zheng, H. Hua, Q. Yang, L. Chen, Y. Xi, C. Hu, Synthesis and photoelectrochemical properties of CdWO₄ and CdS/CdWO₄ nanostructures, Appl. Surf. Sci. 327 (2015) 140–148, <https://doi.org/10.1016/j.apsusc.2014.11.156>.

[62] N. Hashim, P. Natarajan, A.K. Ray, Intrinsic kinetic study for photocatalytic degradation of diclofenac under UV and visible light, Ind. Eng. Chem. Res. 53 (2014) 18637–18646, <https://doi.org/10.1021/ie404355k>.

[63] Y. Tian, W. Li, C. Zhao, Y. Wang, B. Zhang, Q. Zhang, Fabrication of hollow mesoporous SiO₂-BiOCl@PANI@Pd photocatalysts to improve the photocatalytic performance under visible light, Appl. Catal. B 15 (2017) 136–146, <https://doi.org/10.1016/j.apcatb.2017.05.026>.

[64] Q. Zhang, P. Chen, M. Zhuo, F. Wang, Y. Su, T. Chen, K. Yao, Z. Cai, W. Lv, G. Liu, Degradation of indometacin by simulated sunlight activated CDs-loaded BiPO₄ photocatalyst: Roles of oxidative species, Appl. Catal. B 221 (2018) 129–139, <https://doi.org/10.1016/j.apcatb.2017.09.008>.

[65] W. Liu, Y. Li, F. Liu, W. Jiang, D. Zhang, J. Liang, Visible-light-driven photocatalytic degradation of diclofenac by carbon quantum dots modified porous g-C₃N₄: Mechanisms, degradation pathway and DFT calculation, Water Res. 151 (2019) 8–19, <https://doi.org/10.1016/j.watres.2018.11.084>.

[66] Y. Ji, Y. Fan, K. Liu, D. Kong, J. Lu, Thermo activated persulfate oxidation of antibiotic sulfamethoxazole and structurally related compounds, Water Res. 87 (2015) 1–9, <https://doi.org/10.1016/j.watres.2015.09.005>.

[67] P. Calza, V.A. Sakkas, C. Medana, C. Baiocchi, A. Dimou, E. Pelizzetti, T. Albanis, Photocatalytic degradation study of diclofenac over aqueous TiO₂ suspensions, Appl. Catal. B 67 (2006) 197–205, <https://doi.org/10.1016/j.apcatb.2006.04.021>.

[68] C. Martínez, M. Canle L, M.I. Fernández, J.A. Santaballa, J. Faria, Aqueous degradation of diclofenac by heterogeneous photocatalysis using nanostructured materials, Appl. Catal. B 107 (2011) 110–118, <https://doi.org/10.1016/j.apcatb.2011.07.003>.

[69] F. Wang, Y. Wang, Y. Feng, Y. Zeng, Z. Xie, Q. Zhang, Y. Su, C. Ping, L. Yang, K. Yao, Novel ternary photocatalyst of single atom-dispersed silver and carbon quantum dots co-loaded with ultrathin g-C₃N₄ for broad spectrum photocatalytic degradation of naproxen, Appl. Catal. B 221 (2017) 510–520, <https://doi.org/10.1016/j.apcatb.2017.09.055>.

[70] H.S. Wahab, T. Bredow, S.M. Aliwi, A computational study on the adsorption and ring cleavage of para-chlorophenol on anatase TiO₂ surface, Surf. Sci. 603 (2009) 664–669, <https://doi.org/10.1016/j.susc.2009.01.001>.

[71] P. Chen, Q. Zhang, Y. Su, L. Shen, F. Wang, H. Liu, Y. Liu, Z. Cai, W. Lv, G. Liu, Accelerated photocatalytic degradation of diclofenac by a novel CQDs/BiO₂COOH hybrid material under visible-light irradiation: Dechlorination, detoxicity, and a new superoxide radical model study, Chem. Eng. J. 332 (2018) 737–748, <https://doi.org/10.1016/j.cej.2017.09.118>.

[72] X. Yu, R. Du, B. Li, Y. Zhang, H. Liu, J. Qu, X. An, Biomolecule-assisted self-assembly of CdS/MoS₂/graphene hollow spheres as high-efficiency photocatalysts for hydrogen evolution without noble metals, Appl. Catal. B 182 (2016) 504–512, <https://doi.org/10.1016/j.apcatb.2015.09.003>.

[73] P. Chen, F. Wang, Z.-F. Chen, Q. Zhang, Y. Su, L. Shen, K. Yao, Y. Liu, Z. Cai, W. Lv, G. Liu, Study on the photocatalytic mechanism and detoxicity of gemfibrozil by a sunlight-driven TiO₂/carbon dots photocatalyst: the significant roles of reactive oxygen species, Appl. Catal. B 204 (2017) 250–259, <https://doi.org/10.1016/j.apcatb.2016.11.040>.

[74] R. Li, M. Cai, Z. Xie, Q. Zhang, Y. Zeng, H. Liu, G. Liu, W. Lv, Construction of heterostructured CuFe₂O₄/g-C₃N₄ nanocomposite as an efficient visible light photocatalyst with peroxydisulfate for the organic oxidation, Appl. Catal. B 244 (2019) 974–982, <https://doi.org/10.1016/j.apcatb.2018.12.043>.